

# Hot Holographic 2-flavor Quark Star

---

**Le-Feng Chen,<sup>a</sup> Jing-Yi Wu,<sup>b,1</sup> Hao Feng,<sup>a</sup> Tian-Shun Chen,<sup>a</sup> and Kilar Zhang<sup>a,c,d,1</sup>**

<sup>a</sup>*Department of Physics and Institute for Quantum Science and Technology, Shanghai University, Shanghai 200444, China*

<sup>b</sup>*School of Astronomy and Space Science, University of Chinese Academy of Sciences (UCAS), Beijing 100049, China*

<sup>c</sup>*Shanghai Key Lab for Astrophysics, Shanghai 200234, China*

<sup>d</sup>*Shanghai Key Laboratory of High Temperature Superconductors, Shanghai 200444, China*

*E-mail:* [clf@shu.edu.cn](mailto:clf@shu.edu.cn), [wujingyi222@mailsucas.ac.cn](mailto:wujingyi222@mailsucas.ac.cn),  
[fenghaozi@shu.edu.cn](mailto:fenghaozi@shu.edu.cn), [cts2003912@shu.edu.cn](mailto:cts2003912@shu.edu.cn), [kilar@shu.edu.cn](mailto:kilar@shu.edu.cn)

**ABSTRACT:** Applying the holographic 2-flavor Einstein–Maxwell–dilaton model, the parameters of which are fixed by lattice QCD, we extract the equations of state for hot quark–gluon plasma around the critical point at  $T = 182$  MeV, and have corresponding quark star cores constructed. By further adding hadron shells, the mass range of the whole stars spans from 2 to 17 solar masses, with the maximum compactness around 0.22. This result allows them to be black hole mimickers and candidates for gap events. The I–Love–Q–C relations are also analyzed, which show consistency with the neutron star cases when the discontinuity at the quark–hadron interface is not large. Furthermore, we illustrate the full parameter maps of the energy density and pressure as functions of the temperature and chemical potential and discuss the constant thermal conductivity case supposing a heat source inside.

---

<sup>1</sup>Corresponding author.

---

## Contents

<b>1</b>	<b>Introduction</b>	<b>1</b>
<b>2</b>	<b>Holographic 2-Flavor QCD Model</b>	<b>3</b>
<b>3</b>	<b>Hot Quark Stars and Their I–Love–Q–C Relations</b>	<b>6</b>
<b>4</b>	<b>More Discussions on the <math>\epsilon</math> and <math>p</math> Parameter Space</b>	<b>13</b>
<b>5</b>	<b>Conclusions</b>	<b>17</b>

---

## 1 Introduction

How to obtain bare quarks has been a long challenge, since the extreme conditions are almost impossible to realize on the earth. A possible solution may lie in compact stars, like in the cores of neutron stars (NSs).

Gravitational Waves (GWs) offered us a brand new way to detect NSs in the summer of 2017 [1–3], deciphering the information of masses and tidal deformations [4]. Together with a traditional electromagnetic (EM) observation apparatus like NICER [5], we can narrow the windows and place constraints on the NS equation of state (EoS), excluding many EoS candidates. However, observations alone are far from enough to break the degeneracy, and theoretical derivations are needed.

Unfortunately, theoretically obtaining the exact EoS for NSs is still an open question, not to mention quark stars (Qs), require highly non-perturbative quantum chromodynamics (QCDs) beyond the current analysis and calculation power. At this stage, holographic methods [6, 7] provide hopeful approaches to extract the EoS. Two major holographic QCD models originating from string theory, one from brane constructions and the other called Einstein–Maxwell–dilaton (EMD) [8] model, could both lead to competitive EoS candidates.

For brane constructions, as a top-down model, applying D4/D8 brane configurations, namely Witten–Sakai–Sugimoto (WSS) model [6, 9, 10], one can extract NS EoS. On the other hand, D3/D7 configurations can lead to QS EoS.

For QS itself, there are also two scenarios. Low or zero temperature and high density lead to quark matter, but most of the current models (including D3/D7 model) [11–15] do not favor the existence of quark cores, as the stars constructed are unstable. As some exceptions, studies [16–20] have found that stable NS can form with cold quark cores. High temperature and relatively lower density result in quark–gluon plasma, which may form a new type of star [21] rather than NS.

In [22], the holographic EMD model used to describe strongly coupled quark–gluon plasma is reviewed. The EMD model can not only predict transport coefficients, but also

predict the existence of critical endpoint (CEP) in the QCD phase diagram. We adopt a model [23] introduced in this review because its thermodynamic quantities can be obtained through holographic renormalization and thermodynamic relations, thereby extracting the EoS. Ref. [23] is based on the DeWolfe–Gubser–Rosen (DGR) [24] model, and improvements to this model enable 2+1 flavor QCD matter at  $\mu_B = 0$  to quantitatively match the latest lattice data [25, 26], thereby determining the precise coordinates of the critical endpoint at  $(\mu_{CEP}, T_{CEP}) = (555 \text{ MeV}, 105 \text{ MeV})$  and characterizing the first-order transition line. The 2-flavor model [27] adopts the coupling function form obtained from the 2+1-flavor case, using lattice data [28] from simulations performed at bare quark masses corresponding to pion mass  $m_\pi \sim 360 \text{ MeV}$  and  $N_t = 12$ , with  $N_f = 2$  degenerate quark flavor. They set the pseudo-critical temperature from lattice simulations [29] to  $T_c(\mu_B = 0) = 205 \text{ MeV}$  to match the lattice data, which falls within the deconfinement range of  $219 \pm 3 \pm 14 \text{ MeV}$  obtained from [28]. Moreover, the paper [27] calculates the relationship between baryon number density and temperature for different  $\mu_B/T$  ratios. The results show that the holographic predictions match well with the lattice results at low chemical potential [29], which strongly supports the hQCD model we employed. We considered 2 + 1-flavor case in [21], and now we discuss the 2-flavor case.

There are two major differences from the last work. First is, of course, the change in flavors. Constraining to only up and down quarks is, in some sense, more realistic. It is noteworthy that the change in quark flavor number has a very pronounced effect on the CEP position. Applying the same EMD model, in the case of 2+1-flavor, CEP is located at  $(\mu_{CEP}, T_{CEP}) = (219 \text{ MeV}, 182 \text{ MeV})$  [23], while for 2-flavor,  $(\mu_{CEP}, T_{CEP}) = (555 \text{ MeV}, 105 \text{ MeV})$  [27]. The determining procedure is briefly as follows: Through calculations of the temperature dependence of the Polyakov loop and free energy density, the EMD model finds that when  $\mu$  approaches the critical value (219 MeV), the susceptibility of the Polyakov loop becomes infinite. Beyond this critical value, both the Polyakov loop and free energy density exhibit multi-valued behavior, indicating the occurrence of a first-order phase transition, which also determines the position of the CEP. In practice, the form of the potentials (2.2) are the same for both 2+1-flavor and 2-flavor cases, but the coefficients are set differently according to the corresponding lattice data (as illustrated in Table 1 of [27]), thus leading to different CEP. The reason why the 2+1-flavor model is sometimes favored is that the state with a strange quark is considered to be the ground state of baryonic matter at zero temperature in the literature [30]. However, in 2018, there was also a claim that the 2-flavor case can be more stable if the baryon number is more than 300 (although, this is beyond the periodic table) [31]. Those two conclusions are for cold quark matter, while for hot quark–gluon plasma, constraining to only up and down quarks is more natural, without the need of introducing strange quarks.

Secondly, in contrast to previous studies that computed the interior structures of finite-temperature QS and NS models using either the isothermal assumption or other simplified relations [32–34], we now show the whole parameter spaces for  $\epsilon$  and  $p$  as functions of  $T$  and  $\mu$  and, in addition discuss the special curves under constant thermal conductivity.

We end up with hot and massive QS, the masses of which range from 2 to 17  $M_\odot$ , which are much larger than NS, though lower compared to their 2+1-flavor counterparts

with 5 to 30  $M_\odot$  in [21]. This property enables them to mimic black holes (BHs) rather than NS.

For the formation and lifetime of such high temperature stars, similar questions arise like the cases in [21]. In both the early universe and core-collapse supernovae, extreme conditions may generate temperatures sufficient for quark–gluon plasma formation. While supernovae can reach as high as 30–50 MeV [35, 36] in the literature, we suggest that certain extreme explosions could attain temperatures several times higher, to more than 182 MeV, potentially creating hot QS. While hot QS may predict rapid collapse into NS and subsequently BH due to intense thermal radiation, the models in this paper are dealing with a stratified structure featuring a quark-phase core enveloped by neutron-rich matter. Crucially, strong radiation reflection at the phase transition boundary may significantly reduce energy leakage from the quark core, thereby extending the stellar lifespan. Detailed investigation of these interface dynamics and the observational implications will be addressed in future work.

In order to analyze the ability of detections, we calculate the universal relations across the moment of inertia (I), the tidal deformability (Love), and the quadrupole moment (Q) and the compactness (C), which is also called the I–Love–Q–C relations. The relations have been found to be independent on most models, whether the EoS are continuous [37–44] or have small discontinuity [45–49]. As BH mimickers, the stars are distinguishable by comparing the masses with the detection results of NS. Furthermore, the stars can be differentiated from BH using characteristic wave forms and, further, the non-zero tidal love number (TLN) in contrast to the zero TLN of BH in general relativity. The deviations of the I–Love–Q–C relations for different models are also effective in observations. Moreover, the thermal radiation emitted by such high-temperature stars provides traditional methods for their detection.

This paper is organized as follows. Section 1 is the introduction, and Section 2 summarizes the way to extract EoS from the holographic 2-flavor EMD model. Section 3 shows the QS constructed and analyzes their I–Love–Q–C relations. We discuss more on the full parameter space of  $\epsilon$  and  $p$  and consider a constant thermal conductivity case in Section 4. We provide conclusions in Section 5.

## 2 Holographic 2-Flavor QCD Model

Research was conducted within the EMD theoretical framework in five-dimensional space. The action of the system is represented as:

$$S = \frac{1}{2\kappa_N^2} \int d^5x \sqrt{-g} \left[ R - \frac{1}{2} \nabla_\mu \phi \nabla^\mu \phi - \frac{Z(\phi)}{4} F_{\mu\nu} F^{\mu\nu} - U(\phi) \right], \quad (2.1)$$

where  $\kappa_N$  represents the effective Newton constant,  $\phi$  is a scalar field called dilaton, which breaks conformal symmetry,  $F_{\mu\nu}$  is the field strength tensor of the U(1) gauge field, and  $g$  denotes the determinant of the five-dimensional spacetime metric tensor,  $R$  is the Ricci scalar curvature. The scalar potential  $U(\phi)$  and the gauge coupling function  $Z(\phi)$  are chosen to reproduce key features of 2-flavor lattice QCD at zero chemical potential. Based

on the work of [27], we adopt the following forms:

$$\begin{aligned} U(\phi) &= -12 \cosh[c_1 \phi] + (6c_1^2 - \frac{3}{2})\phi^2 + c_2 \phi^6, \\ Z(\phi) &= \frac{\text{sech}[c_4 \phi^3]}{1 + c_3} + \frac{c_3}{1 + c_3} e^{-c_5 \phi}. \end{aligned} \quad (2.2)$$

As established by lattice data in [27], the parameters  $\kappa_N$  and  $c_i$  are determined as the following values:  $\kappa_N^2 = 2\pi(3.72)$ ,  $c_1 = 0.7100$ ,  $c_2 = 0.0002$ ,  $c_3 = 0.530$ ,  $c_4 = 0.085$ , and  $c_5 = 30$ .

The metric form of a five-dimensional AdS black hole with scalar hair is as follows

$$ds^2 = -f(r)e^{-\eta(r)}dt^2 + \frac{dr^2}{f(r)} + r^2(dx^2 + dy^2 + dz^2), \quad (2.3)$$

and

$$\phi = \phi(r), \quad A_t = A_t(r). \quad (2.4)$$

where  $f(r)$  and  $\eta(r)$  are all functions of  $r$ , and  $A_t$  is the  $t$ -component of the gauge field.

The temperature  $T$  and entropy density  $s$  can both be obtained from the horizon

$$T = \frac{1}{4\pi} f'(r_h) e^{-\eta(r_h)/2}, \quad s = \frac{2\pi}{\kappa_N^2} r_h^3, \quad (2.5)$$

where  $r_h$  is the horizon radius.

Through the calculation method in [23], the specific form of energy density  $\epsilon$  and pressure  $p$  can be obtained

$$\begin{aligned} \epsilon &= \frac{1}{2\kappa_N^2} (-3f_v + \phi_s \phi_v + \frac{1 + 48b}{48} \phi_s^4), \\ p &= \frac{1}{2\kappa_N^2} (-f_v + \phi_s \phi_v + \frac{3 - 48b - 8c_1^4}{48} \phi_s^4), \end{aligned} \quad (2.6)$$

where  $f_v$ ,  $\phi_s$ ,  $\phi_v$  are the parameters in the asymptotic expansion of the metric function on the AdS boundary, and  $b = -0.25707$  is the result from holographic renormalization. The  $\phi_s$  originates from the asymptotic expansion of scalar fields, and their non-zero values break the conformal symmetry. Additionally, the value of  $\phi_s = 1.227$  GeV [27] can be fixed through lattice QCD.

To obtain the mass and the radius of the star through solving Tolman–Oppenheimer–Volkoff (TOV) equations with the EoS, we need to convert the usual QCD units [MeV<sup>4</sup>] into the so-called astronomical units  $r_\odot$ ,  $\epsilon_\odot$ ,  $p_\odot$ , with  $r_\odot = G_N M_\odot / c^2$ ,  $\epsilon_\odot = M_\odot / r_\odot^3$ , and  $p_\odot = c^2 \epsilon_\odot$ ,

$$\epsilon_\odot = p_\odot = 6.60271 \times 10^{14} \text{ MeV}^4 = 3.14644 \times 10^5 \text{ MeV} \cdot \text{fm}^{-3}, \quad (2.7)$$

where we have taken  $c = G_N = 1$ .

In [27], they obtained the critical end point (CEP) of 2-flavor QCD ( $\mu = 219$  MeV,  $T = 182$  MeV). For simplified analysis, we selected five sets of data points around CEP, which are  $\mu/T = 1$ ,  $\mu/T = 1.2033$ ,  $\mu/T = 1.25$ ,  $T = 182$  MeV and  $\mu = 219$  MeV,

and performed fittings on these data, with the fitting results and data shown in Figure 1. The real EoS will be contained within this range, though complicated to obtain directly.

We must emphasize that the blue data points in Figure 1 do not reach zero because we select the high-temperature quark–gluon plasma, in which case neither pressure nor temperature is zero.

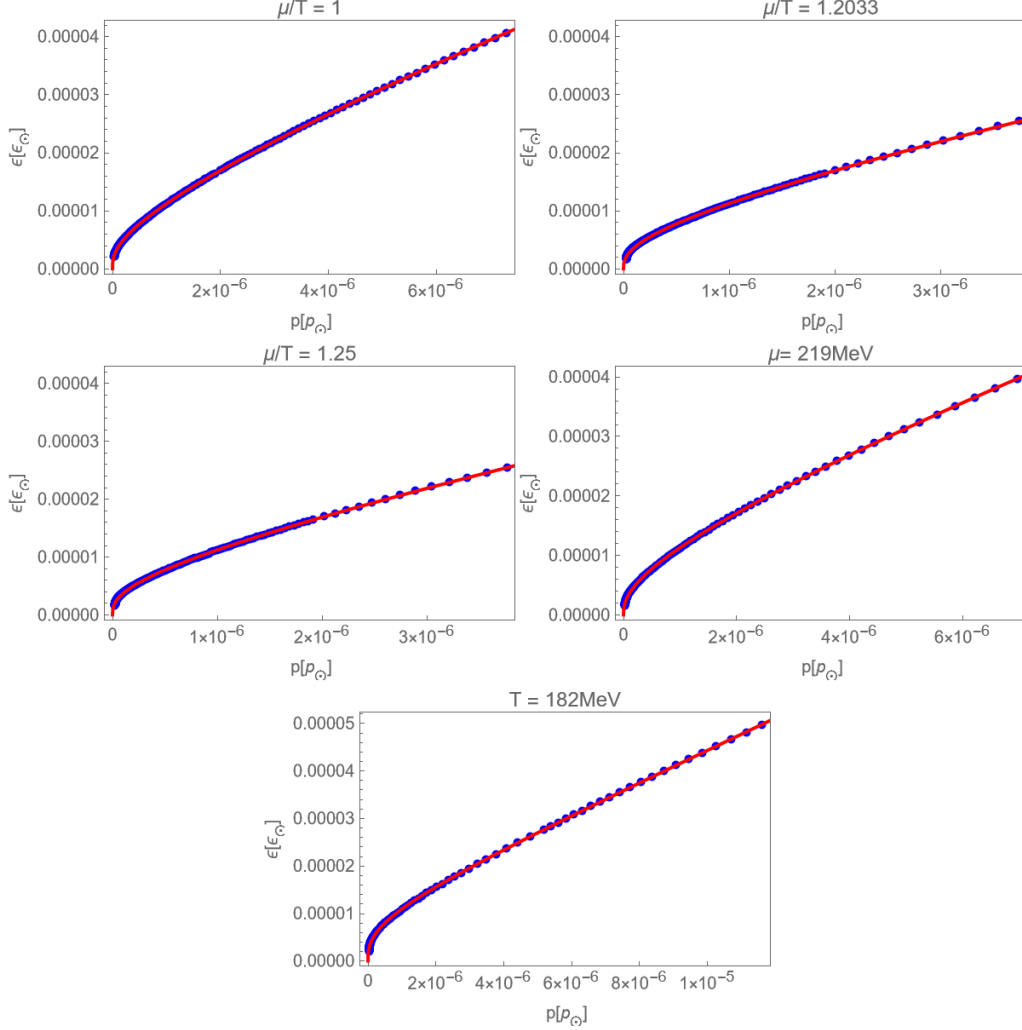


**Figure 1:** Energy–pressure data and fitted curves under five different  $T, \mu$  conditions. Blue points represent numerical data, and red lines are fitted curves. Here, our data does not reach zero because this is high-temperature quark matter, which still maintains a certain pressure at the phase transition point.

The fitting results corresponding to different physical conditions are listed below:  $p_1, \epsilon_1$  for  $\mu/T = 1$ ,  $p_2, \epsilon_2$  for  $\mu/T = 1.2033$ ,  $p_3, \epsilon_3$  for  $\mu/T = 1.25$ ,  $p_4, \epsilon_4$  for  $T = 182 \text{ MeV}$ ,  $p_5, \epsilon_5$

for  $\mu = 219$  MeV.

$$\begin{aligned}\epsilon_1 &= 0.000501863 p_1^{0.315468} + 1.15292 p_1^{0.89651}, \\ p_1 &\in [3.0918 \times 10^{-8}, 7.3047 \times 10^{-6}], \\ \epsilon_1 &\in [2.1682 \times 10^{-6}, 4.066 \times 10^{-5}],\end{aligned}\tag{2.8}$$

$$\begin{aligned}\epsilon_2 &= 0.00139264 p_2^{0.375067} + 2.6989 p_2^{0.982421}, \\ p_2 &\in [2.627 \times 10^{-8}, 7.3045 \times 10^{-6}], \\ \epsilon_2 &\in [1.7023 \times 10^{-6}, 4.0658 \times 10^{-5}],\end{aligned}\tag{2.9}$$

$$\begin{aligned}\epsilon_3 &= 0.000928211 p_3^{0.349754} + 2.15744 p_3^{0.958067}, \\ p_3 &\in [2.3732 \times 10^{-8}, 7.35366 \times 10^{-6}], \\ \epsilon_3 &\in [1.6962 \times 10^{-6}, 4.08 \times 10^{-5}],\end{aligned}\tag{2.10}$$

$$\begin{aligned}\epsilon_4 &= 0.00117483 p_4^{0.350591} + 11.3855 p_4^{1.13679}, \\ p_4 &\in [2.61368 \times 10^{-8}, 1.1615 \times 10^{-5}], \\ \epsilon_4 &\in [2.1067 \times 10^{-6}, 4.9673 \times 10^{-5}],\end{aligned}\tag{2.11}$$

$$\begin{aligned}\epsilon_5 &= 0.001427 p_5^{0.378816} + 2.09627 p_5^{0.958741}, \\ p_5 &\in [2.60394 \times 10^{-8}, 6.97167 \times 10^{-6}], \\ \epsilon_5 &\in [1.5845 \times 10^{-6}, 3.967 \times 10^{-5}].\end{aligned}\tag{2.12}$$

The permissible fitting ranges for pressure ( $p$ ) and energy density ( $\epsilon$ ) in astrophysical units are constrained as follows: the minimum values correspond to the phase transition threshold, whereas the maximum values are determined by stellar stability requirements.

### 3 Hot Quark Stars and Their I–Love–Q–C Relations

Theoretically inferred models play a crucial role in supporting astrophysical observations by leveraging universal relations among key macroscopic properties of compact stars—namely, the I–Love–Q trio [37, 38]. These nearly EoS-independent relations enable the extraction of fundamental stellar parameters from gravitational wave and pulsar timing observations, providing a powerful tool for probing the internal structure and composition of compact objects, including NS and QS.

In Figure 2, we plot the mass–radius (M–R) curve and the I–Love–Q–C relations of the models in Equations (2.8)–(2.12) with the calculation procedures in [38]. We plot the  $\epsilon$  and  $p$  with TOV units  $\epsilon_\odot$  and  $p_\odot$  while the I–Love–Q–C are dimensionless. We should note that, as shown in Figure 1, the pressure of the quark phase is nonzero, but for the simplest analysis, we extend the fitting of the models to  $p = 0$  as the surface condition required, so that the hadron crust shares the same EoS curve (with a smooth phase transition), and we use the terminology “simple” to represent the models. For comparison, we plot the I–Love–Q–C relations for a single polytropic NS model

$$\epsilon_n = \kappa_n p^{\gamma_n},\tag{3.1}$$

with the black dotted curve. Here,  $\gamma_n$  is set to 0.5 as a typical reference and the corresponding  $\kappa_n = 0.09$ , which satisfies the constraint that the maximum mass of NS is about  $2.2 M_\odot$ , which are also the parameters used in [50]. From Figure 2, we observe that the maximum masses of the quark models can reach up to  $17 M_\odot$ . In sight of the panels of the I–Love–Q trio, we find the models still obey the universal relations, compared with the NS model. But for the curves about the compactness, the universality is broken. We regard the deviations as plausible because there exist differences between the unrealistic NS EoS and the realistic ones [38].

More realistically than the “simple” EoS cases, we introduce the “combined” cases: considering that the quark–gluon plasma cools down as it approaches the surface and eventually undergoes a phase transition, we connect the quark cores with the hadron (probably, neutron) crusts at their respective minimum pressures. The hadron model we use is Equation (3.1) with a fixed  $\gamma_n = 0.5$ . At the transition point, we set

$$\epsilon_n(p_t) = m \epsilon_q(p_t), \quad (3.2)$$

to illustrate the discontinuities. Here,  $\epsilon_q$  is referred to as the energy density of the quark cores, and  $p_t$  represents the transition point. The parameter  $\kappa_n$  depends on the choice of  $m$ .

We plot the EoS, M–R relations and I–Love–Q–C relations for “combined” QS with  $m = 1, 1.2, 0.8$  and  $0.5$  in Figures 3–6 through the procedures for the two-layer models in [51]. In the panels for M–R relations, we show that the “combined” QS have more unstable components (i.e., the higher radii parts of the stars) for the larger phase transitions, while the stability judging methods can be seen in [52]. We should mention that the selection of the ranges of the central pressure  $p_0$ , which are the initial conditions when solving TOV equations to derive the mass and radius, are the same across all “combined” QS for the respective quark EoS. Through the trend of instability with the phase transition, we can foresee that the stars will not exist in extreme circumstances. From the lower six panels, we observe that the I–Love–Q relations are valid for all the “combined” cases. The I–C, Love–C and Q–C curves obey the universality except for  $m = 0.5$ , which may be induced by the larger phase transition. Compared with Figure 2, the relations for the “combined” cases conform better. The reason is the influence from the hadron shells, which is more dominant for the universality than the cores [38, 50].

Compared with the 2+1-flavor model [21], we obtain nearly half of the masses of the stars from the present models, correspondingly with half of the radii. Furthermore, the universal relations of the 2-flavor models seem to deviate from the referred NS model less than our previous work. The result reduces the mass gaps between NS and the QS in our previous work. We think the observations on the 2-flavor QS are able to supply the formation theories of the compact stars.

The ranges of the masses of the “simple” QS and “combined” cases enable these compact objects to emulate the observable properties of stellar-mass BH. The present study demonstrates that the I–Love–Q–C universal relations remain valid across a broad class of “combined” configurations, thereby reinforcing their applicability beyond 2-flavor quark matter systems. From an observational perspective, these universal relations may serve as a



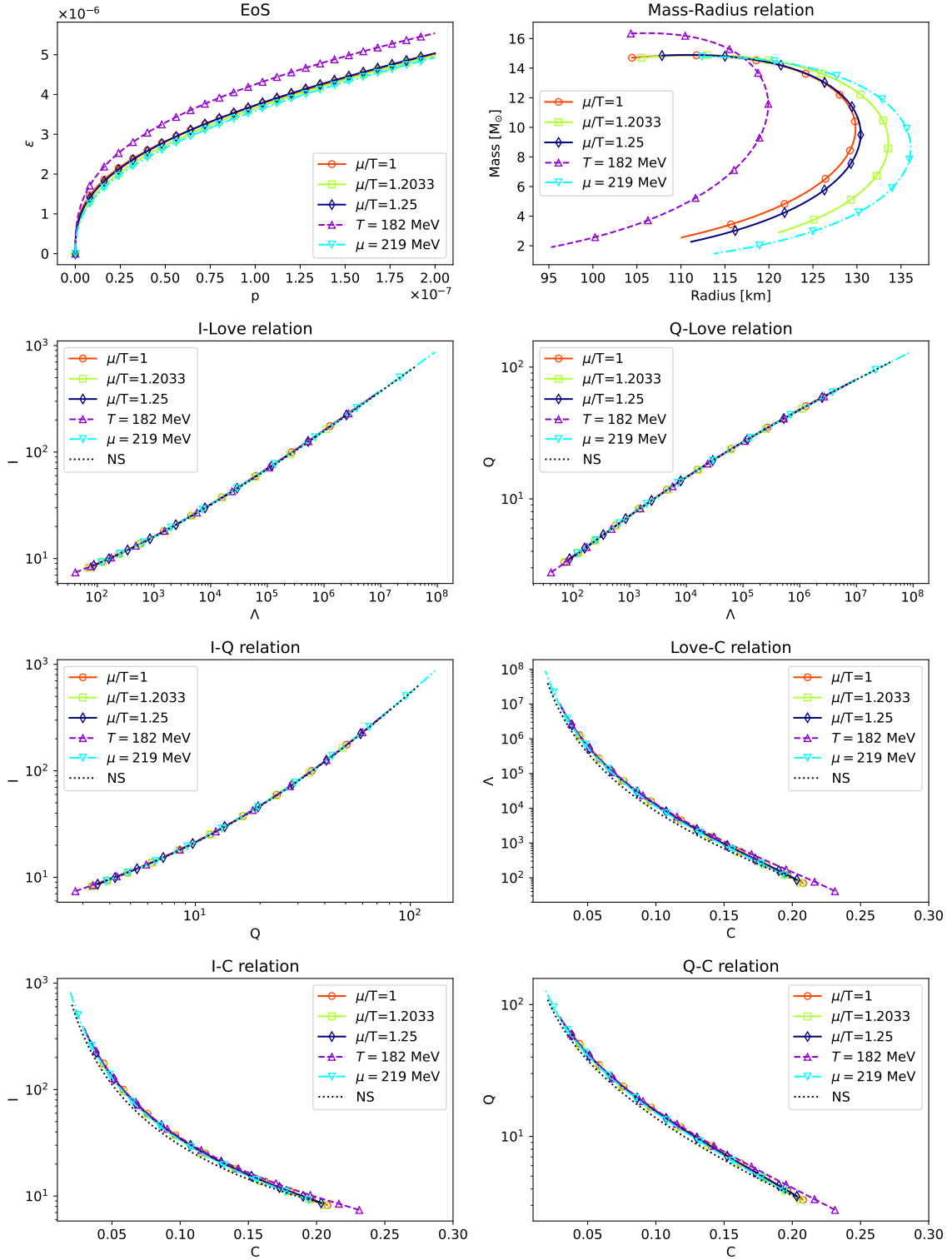


**Figure 2:** The EoS, M–R relation, and I–Love–Q–C relations for the “simple” QS are presented using various models described in Equations (2.8)–(2.12). For comparison, the panels showing the I–Love–Q–C relations of a polytropic NS, given by  $\epsilon_n = 0.09p_n^{0.5}$ , is plotted with a black dotted line.

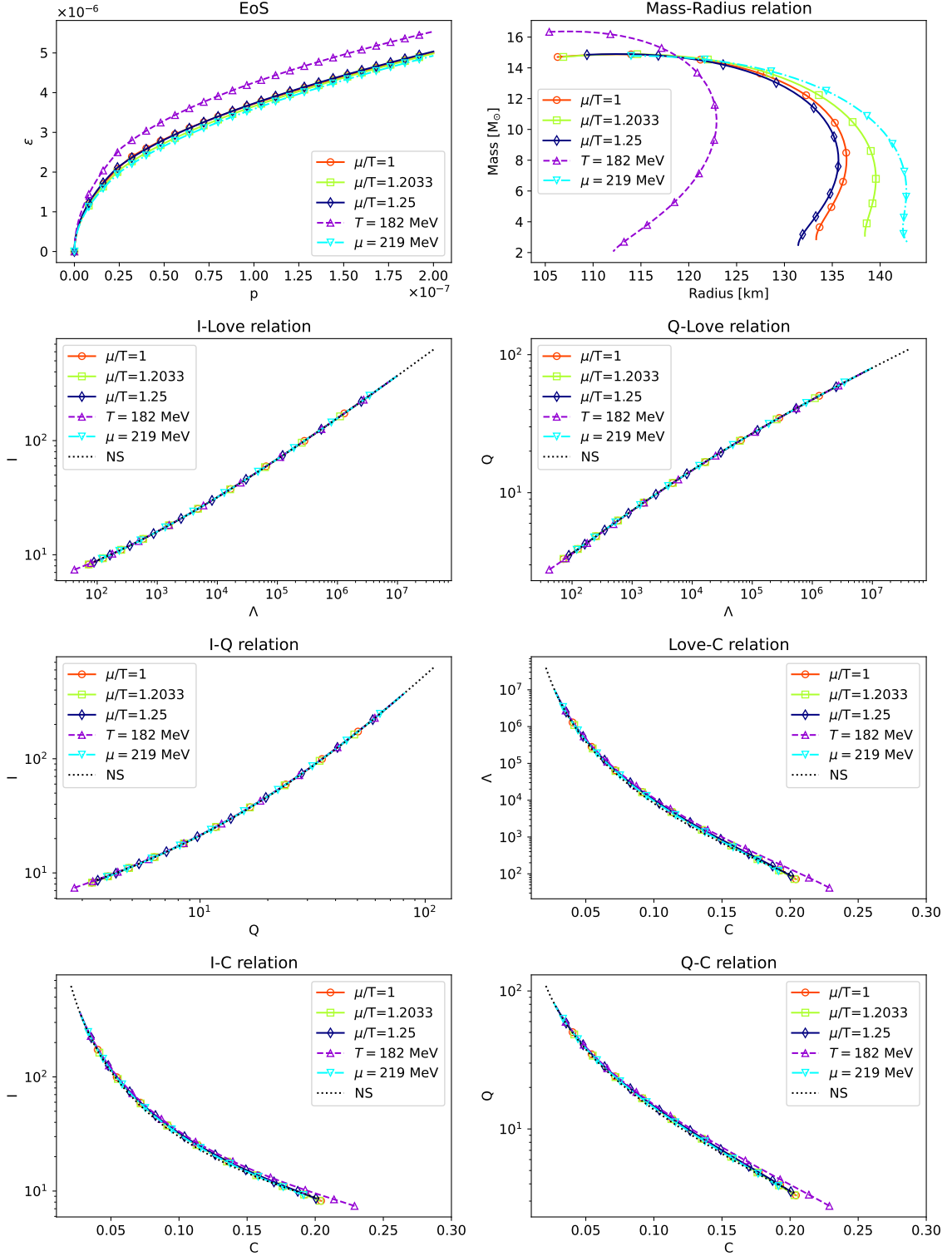


**Figure 3:** The EoS, M-R relation, and I-Love-Q-C relations for the “combined” QS consisting of quark cores and hadron shells with  $m = 1$  in Equation (3.2). For comparison, the I-Love-Q-C relations of a polytropic NS, given by  $\epsilon_n = 0.09p_n^{0.5}$ , are plotted with a black dotted line.

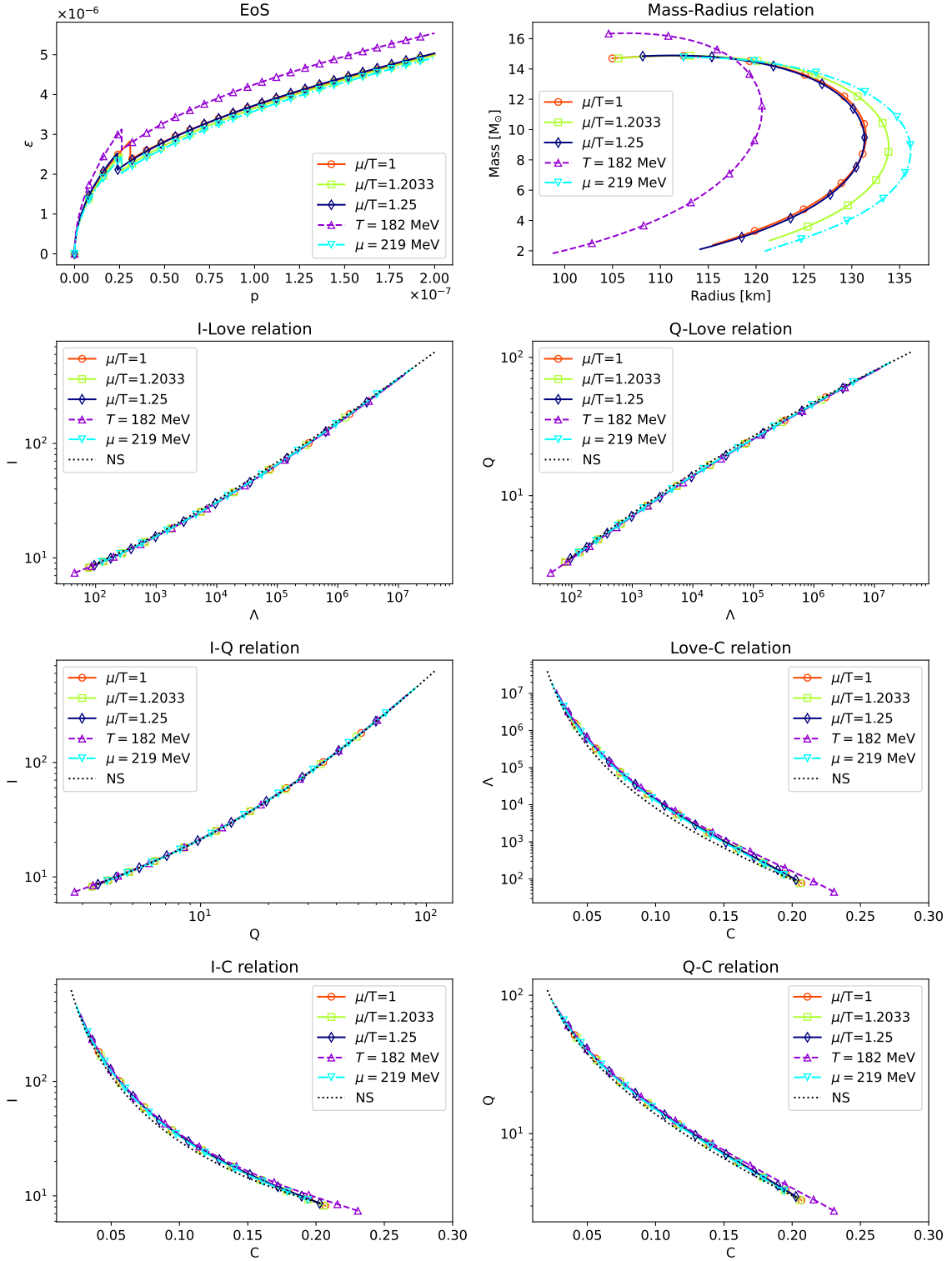


**Figure 4:** The EoS, M–R relation, and I–Love–Q–C relations for the “combined” QS consisting of quark cores and hadron shells with  $m = 1.2$  in Equation (3.2). For comparison, the I–Love–Q–C relations of a polytropic NS, given by  $\epsilon_n = 0.09p_n^{0.5}$ , are plotted with a black dotted line.

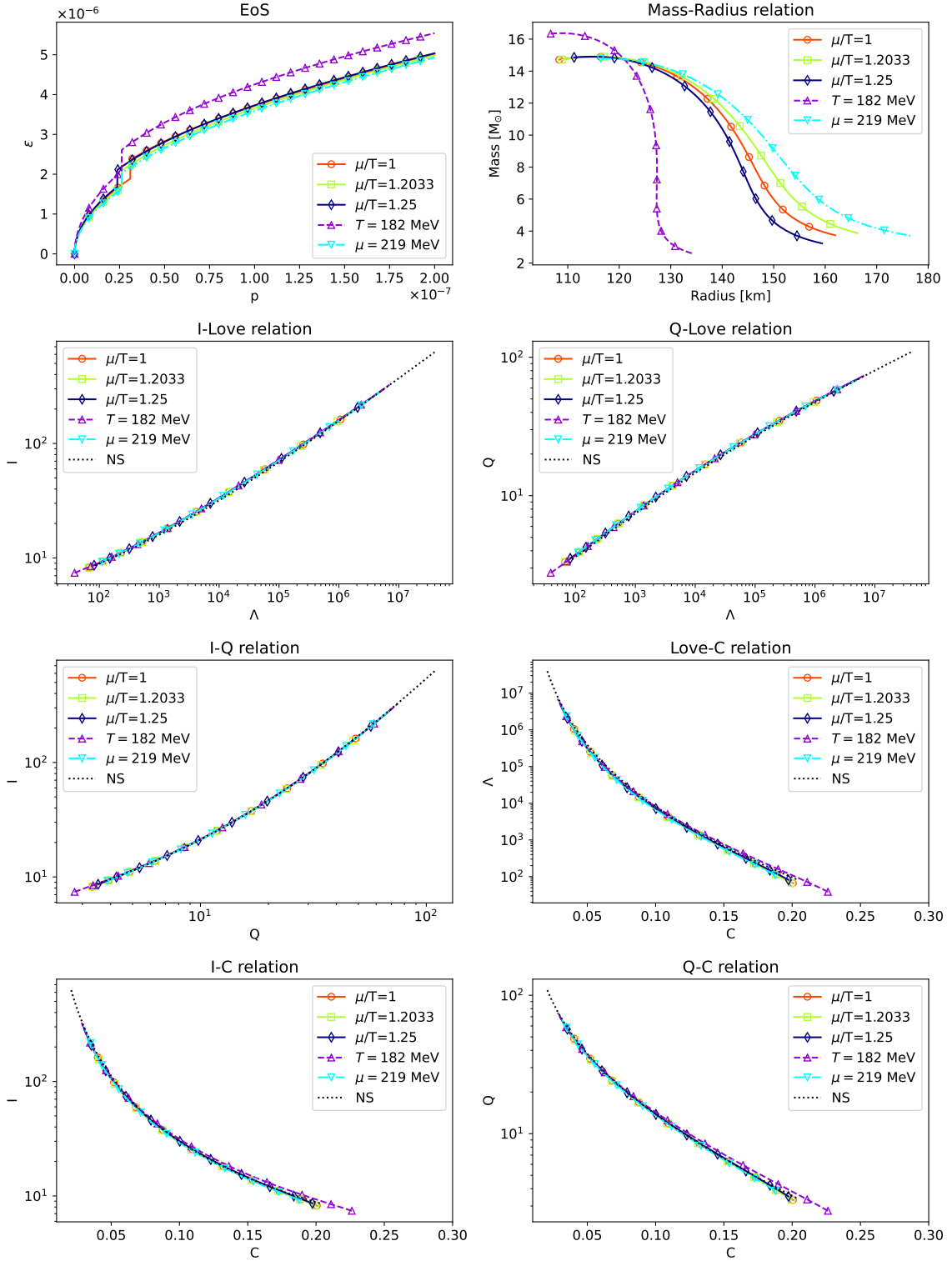


**Figure 5:** The EoS, M–R relation, and I–Love–Q–C relations for the “combined” QS consisting of quark cores and hadron shells with  $m = 0.8$  in Equation (3.2). For comparison, the the I–Love–Q–C relations of a polytropic NS, given by  $\epsilon_n = 0.09p_n^{0.5}$ , are plotted with a black dotted line.

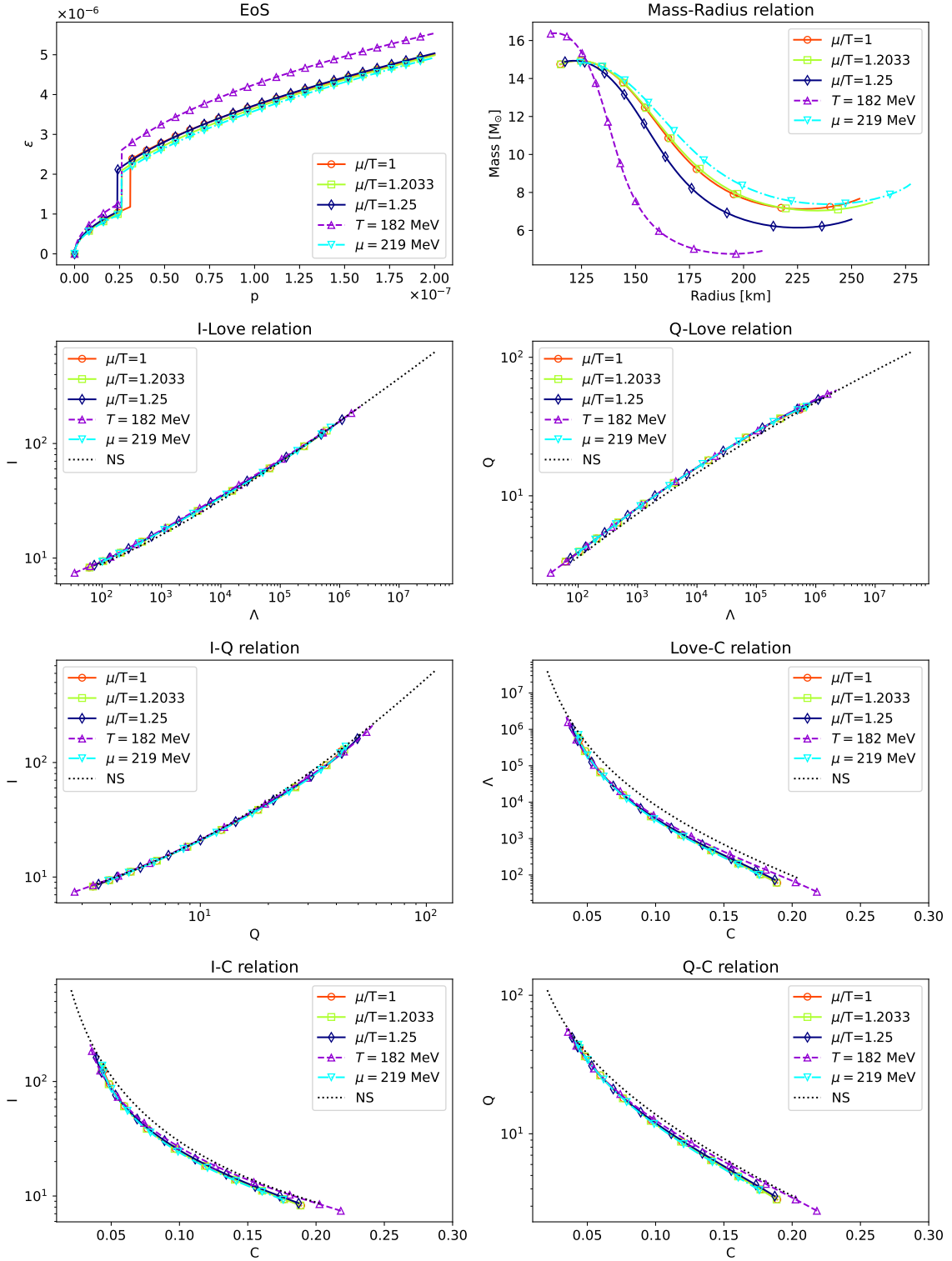


**Figure 6:** The EoS, M–R relation, and I–Love–Q–C relations for the “combined” QS consisting of quark cores and hadron shells with  $m = 0.5$  in Equation (3.2). For comparison, the I–Love–Q–C relations of a polytropic NS, given by  $\epsilon_n = 0.09p_n^{0.5}$ , are plotted with a black dotted line.

diagnostic tool to discriminate between BH and QS, particularly due to the vanishing TLN of BH in general relativity. Additionally, the observed deviations in compactness-related relations may offer potential insights into holographic quark matter models. Importantly, observations of “combined” QS could constrain the parameters governing the phase transition between deconfined quark matter and hadronic matter, thereby offering a pathway to probe the microphysics of dense matter in astrophysical environments.

#### 4 More Discussions on the $\epsilon$ and $p$ Parameter Space

In this section, we illustrate the whole  $\epsilon$  and  $p$  parameter space, and also consider a more complicated case study by replacing the previous simple conditions on  $\mu$  and  $T$  (as discussed in Section 2) with a constant thermal conductivity constraint.

First, we numerically determine the relationships  $\epsilon(\mu, T)$  and  $p(\mu, T)$  using a holographic 2-flavor QCD model, presenting these correlations as heatmaps in Figure 7.

This visualization displays all the EoS information for the quark phase of a holographic 2-flavor QCD model, expressing pressure  $p$  and energy density  $\epsilon$  as functions of chemical potential  $\mu$  and temperature  $T$ . The color gradient quantitatively indicates the values of these thermodynamic quantities. Our investigation concentrates solely on the quark-dominated regime situated above the first-order transition boundary. In the diagram, the shaded gray area corresponds to the hadronic matter domain, with both the CEP and first order line taken from reference [27].

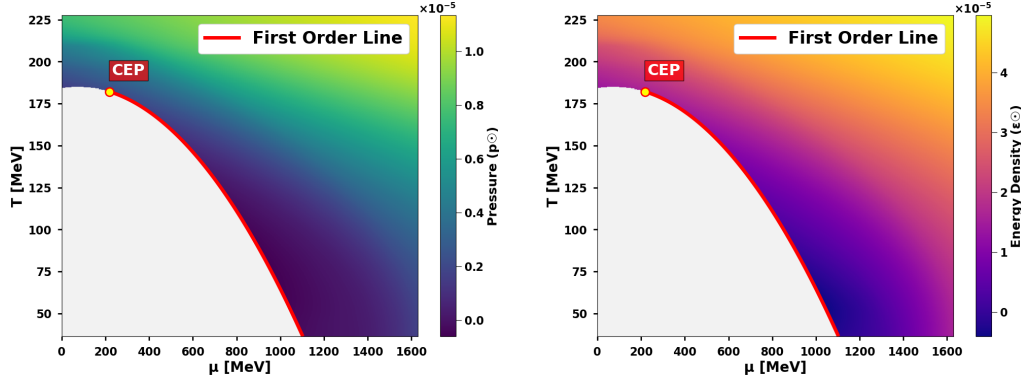


**Figure 7:** The heatmap presents all the  $T, \mu$  dependence for  $p$  and  $\epsilon$  of the Holographic 2-flavor QCD Model (notice that here for  $p$  and  $\epsilon$  we are using astronomical units  $p_\odot$  and  $\epsilon_\odot$  for later convenience, rather than QCD units):  $p = p(\mu, T)$  and  $\epsilon = \epsilon(\mu, T)$ , where the shading of the background color represents the magnitudes of  $p$  and  $\epsilon$ . The CEP and first-order line are taken from reference [27].

Typically, realistic conditions assume rapid attainment of thermal equilibrium, corresponding to the constant-temperature stellar scenario already addressed in the preceding discussion of  $T = \text{constant}$ . We now turn to the next simplest non-trivial configuration—a stellar body with constant thermal conductivity containing a thermal reservoir in the center, which will be our focus in the following analysis.

Although theoretically the thermal conductivity of each point in the  $(\mu, T)$  parameter space could be derived from holographic principles, we defer the complete holographic analysis to future work. For computational simplicity, we instead solve the TOV equations starting from static field equations under constant thermal conductivity conditions. The temperature profile of QS is combined with the  $\mu$ - and  $T$ -dependent expressions of energy density ( $\epsilon$ ) and pressure ( $p$ ) to obtain solutions, followed by a discussion of key results.

The temperature distribution in stars with constant thermal conductivity satisfies the Laplace equation:

$$\nabla^2 T = 0. \quad (4.1)$$

Under assumptions of spherical symmetry, the solution takes the form  $T = C/R$ . However, this formulation does not yield a finite central temperature. To resolve this divergence, we introduce a cutoff at radius  $R = R_c$ , establishing the temperature profile:

$$T(r) = \begin{cases} T_0 & r \leq R_c \\ \frac{T_0 R_c}{r} & r > R_c. \end{cases} \quad (4.2)$$

Here, we suppose that the core region ( $r \leq R_c$ ) contains a constant-temperature heat source where the temperature field is not governed by the Laplace equation.

Substituting  $T(r)$  into  $p(\mu, T)$  yields  $\mu(p, r)$ , which when combined with  $\epsilon(T, \mu)$  produces  $\epsilon(p, r)$ . This relationship serves as the EoS for TOV equation integration.

Figure 8a shows the evolutionary paths of  $\mu(T)$  under TOV equation integration for different central initial conditions  $(\mu_0, T_0)$  near the phase transition boundary with  $R_c = 30$  km and 40 km. The pentagrams denote the integration starting points (stellar centers), while the crosses mark the termination points at the phase transition interface.

Notably, different initial conditions lead to distinct integration paths, which means that our approach differs fundamentally from classical solutions as the EoS becomes dependent on central temperature  $T_0$ . Consequently, each QS requires a unique EoS, rendering traditional NS analysis methods (e.g., M–R curve stability criteria) inapplicable here.

We further investigate the  $R_c \rightarrow 0$  limit to eliminate core effects in Figure 8b. In this regime, the quark phase radius contracts proportionally with  $R_c$ , leading to constant pressure where  $\mu(T)$  reduces to an isobaric curve. Remarkably, sufficiently compact stars exhibit pressure-dominated behavior regardless of thermal profile, rendering the constant thermal conductivity condition trivial in this limit.

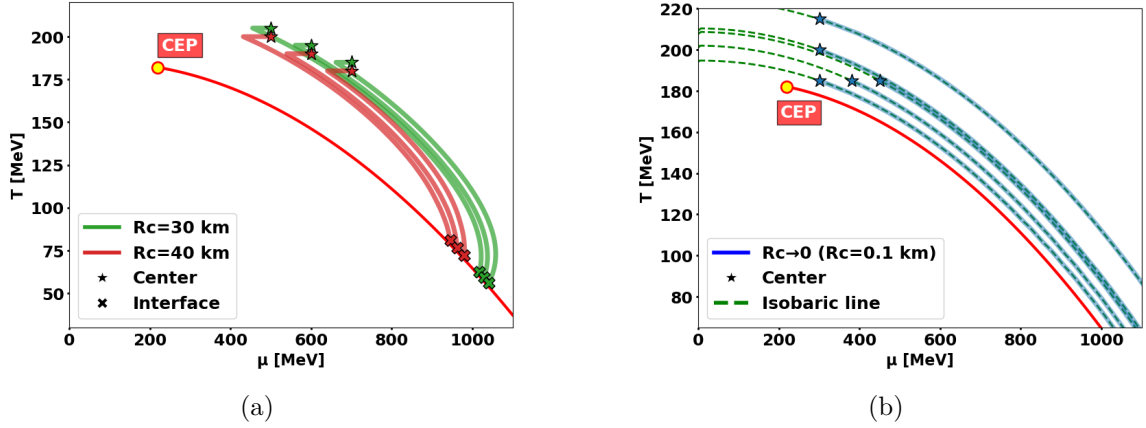


**Figure 8:** Paths of chemical potential and temperature  $(\mu, T)$  as functions of radius for different thermal core radius  $R_c$ : (a) Finite thermal core radius: As radius  $r$  increases, the path intersects the phase transition line and terminates at the stellar interface. Different central conditions  $(\mu_0, T_0)$  correspond to distinct trajectories, reflecting variations in the stellar EoS. (b) Infinitesimal core ( $R_c \rightarrow 0$ ): The pressure remains approximately constant during radial expansion, resulting in an isobaric trajectory.

For physical QS, the central temperature  $T_0$  and chemical potential  $\mu_0$  must satisfy constraints derived from matching to hadron phase exteriors. We adopt the same method as above by connecting to the external hadron shell EoS  $\epsilon_n = \kappa_n p^{\gamma_n}$  (with  $\gamma_n = 0.5$ ) beyond the phase transition boundary.

Figure 9 presents radial profiles of physical quantities for a single star of the complete QS model with  $R_c = 10$  km and central parameters  $(T_0, \mu_0) = (200 \text{ MeV}, 500 \text{ MeV})$ . For simplicity, but enough to illustrate the idea, we select the case with an energy density jump factor of  $m = 1$ , which implies that the energy density is continuous at the phase transition. Then the constructed QS has the quark core radius  $R_t \approx 53$  km, and the total radius is 128 km, while the total mass is  $12.7 M_\odot$ , which is indeed well within the range spanned by the five different EoS cases in Section 2.

Figure 9a–c, radial profiles of pressure, cumulative mass, and energy density. The blue dashed curves denote contributions from the external hadron shell. Due to the imposed energy density jump factor  $m = 1$  at the interface, both pressure and cumulative mass remain smooth across the phase transition boundary. Discontinuities in derivatives of the energy density occur at  $R_c$  and the phase transition interface.

Figure 9d,e, the radial profiles of temperature  $T$  and chemical potential  $\mu$  within the star. The temperature  $T$  strictly follows the distribution of (4.2). We truncate our calculations of  $T$  and  $\mu$  at the interface  $R_t$ , since the EoS of the external hadronic phase is described by a simple single polytrope, where the dependencies of  $T$  and  $\mu$  are not explicitly assigned.

Within  $R_c$ , the temperature is uniform, but the chemical potential  $\mu$  decreases along the constant  $T_0$  line due to the pressure gradient term in the TOV equations. Beyond  $R_c$ ,  $\mu$  initially increases but slightly decreases near the interface, intersecting the phase transi-



tion line.

Figure 9f, EoS of the star showing  $p(\epsilon)$  at different radii. The blue segment corresponds to the external single-polytropic NS EoS.

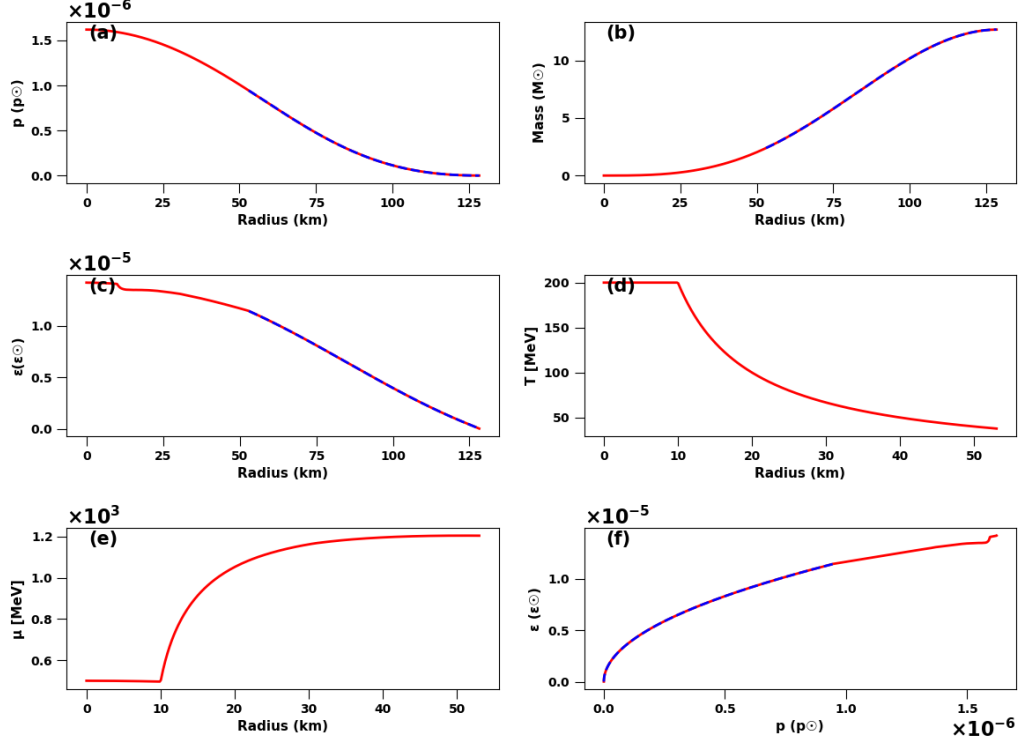


**Figure 9:** Radial profiles of physical quantities for a complete QS model with  $R_c = 10$  km and central parameters  $(T_0, \mu_0) = (200 \text{ MeV}, 500 \text{ MeV})$ . (a) Pressure, (b) mass accumulation, (c) energy density, (d) temperature, (e) chemical potential, and (f) EoS. Blue dashed curves denote contributions from the external single-polytropic hadron matter EoS with  $\gamma_n = 0.5$ , while red curves represent contributions from the internal quark matter.

Under the condition of constant thermal conductivity, this section constructs the temperature- and chemical-potential-dependent EoS via a holographic two-flavor QCD model and investigates the thermodynamics of QS through “combined” configurations with phase transition interfaces. Key findings highlight the unique EoS dependence on the central temperature  $T_0$  and the limiting behavior as  $R_c \rightarrow 0$ .

In the model of this section, to circumvent the divergence of the central temperature, we introduced a central thermal core. However, we observed that its limiting case corresponds to a degenerate solution. Although the model yields an approximate well-behaved conclusion, more precise results should be derived from a holographic framework in future studies.

## 5 Conclusions

We extract the EoS for the 2-flavor quark–gluon plasma at a high temperature using a holographic QCD model. Since the real EoS is a complicated function of chemical potential and temperature, we select five different combinations of  $\mu$  and  $T$  near CEP for simplified analysis and employ them as the core of QS, which would be enough to enclose the real EoS and offer a quick estimation for the possible range.

We first derive the M–R and the I–Love–Q–C relations with the “simple” 2-flavor quark EoS, which are analytical continuations of the fitting curves truncated at the phase transition points. Further to be more realistic and to make comparisons, we pay attention to “combined” QS: connecting the quark cores with polytropic hadron shells under different phase transitions and subsequently apply the “combined” cases to calculate the universal relations.

The results reveal that the mass distribution of both the “simple” and the “combined” QS are above  $2 M_\odot$ , which enables them to be BH mimickers. But the different wave forms and zero TLN of BH in the general relativity can help distinguish the QS from BH. The mass and radius combinations we obtain from the 2-flavor EoS are much different from those from the 2+1-flavor models [21], providing a method to infer the fundamental compositions of the hot QS. Compared with the NS, the I–Love–Q relations remain valid for the “simple” QS and the “combined” cases except for the  $m = 0.5$  model, extending the universal relations for both the continuous and the small discontinuous EoS. The relations about compactness deviate more from each model than the I–Love–Q relations, providing us an effective method to constrain the phenomenological models with phase transitions.

From Figures 2–6, it can be observed that quark stars exhibit a broad mass coverage spanning from about 2 to  $17 M_\odot$ , including the  $2.5\text{--}5 M_\odot$  range, which may effectively interpret the so-called mass gap. Another very interesting outcome is that the minimum mass of QS (determined by the lowest pressure at the phase transition) approximates  $2 M_\odot$ . Below this threshold mass, hot QS would undergo a phase transition to pure hot NS. This critical mass closely aligns with the upper mass limit of NS, which should not be a pure coincidence. In fact, this shows consistency with the results in the literature [11–15] that quark matter is not favored inside NS. If one wants to obtain QS, the masses should exceed  $2 M_\odot$ , in addition to very high temperature. Unlike QS, hot NS lack a radiation-reflecting interface, leading to rapid cooling processes and result in normal cold NS under  $2 M_\odot$ . This thermal characteristic could explain the observational absence of hot NS possessing radii as large as those predicted in our result.

An important new result of this work is presented in Figure 7, though not emphasized extensively, where we numerically determine all the  $T$ ,  $\mu$  dependence for  $p$  and  $\epsilon$  of the quark phase in a holographic 2-flavor QCD model, presented as heatmaps spanning the entire parameter space.

Finally, we also discuss the temperature- and chemical-potential-dependent EoS under constant thermal conductivity with a heat source. Starting from the Laplace equation and combined with the analysis of phase transition interfaces in QS, we reveal the thermodynamic properties of QS under this condition. It highlights the EoS dependence on

the central temperature  $T_0$  and the limiting behavior as  $R_c \rightarrow 0$ , providing insights for potential future investigations.

Considering the model we refer to is based on lattice data with matched bare quark masses and a crossover temperature of  $T_c(\mu_B = 0) = 205$  MeV, whereas recent study [53] obtained a QCD phase transition line result based on lattice data with physical quark masses and a crossover temperature of  $T_c(\mu_B = 0) = 158$  MeV, we can use this model to fix parameters and potentially obtain a more realistic EoS, which will be left for future work.

## Acknowledgments

The authors thank Chian-Shu Chen, Alessandro Parisi, Niko Jokela, Yi-Zhong Fan, Qiyuan Pan, Shao-Feng Ge and an anonymous friend for very helpful suggestions and discussions. K.Z. (Hong Zhang) is supported by a classified fund from Shanghai city.

## References

- [1] Abbott, B.P.; Abbott, R.; Abbott, T.; Acernese, F.; Ackley, K.; Adams, C.; Adams, T.; Addesso, P.; Adhikari, R.X.; Adya, V.B.; et al. GW170817: Observation of Gravitational Waves from a Binary Neutron Star Inspiral. *Phys. Rev. Lett.* **2017**, *119*, 161101. [[CrossRef](#)] [[PubMed](#)]
- [2] Abbott, B.P.; Abbott, R.; Abbott, T.D.; Acernese, F.; Ackley, K.; Adams, C.; Adams, T.; Addesso, P.; Adhikari, R.X.; Adya, V.B.; et al. Properties of the binary neutron star merger GW170817. *Phys. Rev. X* **2019**, *9*, 011001. [[CrossRef](#)]
- [3] Abbott, B.P.; Abbott, R.; Abbott, T.D.; Abraham, S.; Acernese, F.; Ackley, K.; Adams, C.; Adhikari, R.X.; Adya, V.B.; Affeldt, C.; et al. GW190425: Observation of a Compact Binary Coalescence with Total Mass  $\sim 3.4M_\odot$ . *Astrophys. J. Lett.* **2020**, *892*, L3. [[CrossRef](#)]
- [4] Hinderer, T. Tidal Love numbers of neutron stars. *Astrophys. J.* **2008**, *677*, 1216–1220. [[CrossRef](#)]
- [5] Miller, M.C.; Lamb, F.K.; Dittmann, A.J.; Bogdanov, S.; Arzoumanian, Z.; Gendreau, K.C.; Guillot, S.; Ho, W.C.G.; Lattimer, J.M.; Loewenstein, M.; et al. The Radius of PSR J0740+6620 from NICER and XMM-Newton Data. *Astrophys. J. Lett.* **2021**, *918*, L28. [[CrossRef](#)]
- [6] Witten, E. Anti-de sitter space, thermal phase transition, and confinement in gauge theories. *arXiv* **1998**, arXiv:hep-th/9803131.
- [7] Polchinski, J.; Strassler, M.J. The String dual of a confining four-dimensional gauge theory. *arXiv* **2000**, arXiv:hep-th/0003136.
- [8] Gibbons, G.W.; Maeda, K.-i. Black Holes and Membranes in Higher Dimensional Theories with Dilaton Fields. *Nucl. Phys. B* **1988**, *298*, 741–775. [[CrossRef](#)]
- [9] Sakai, T.; Sugimoto, S. Low energy hadron physics in holographic QCD. *Prog. Theor. Phys.* **2005**, *113*, 843–882. [[CrossRef](#)]
- [10] Sakai, T.; Sugimoto, S. More on a holographic dual of QCD. *Prog. Theor. Phys.* **2005**, *114*, 1083–1118. [[CrossRef](#)]

- [11] Hoyos, C.; Fernández, D.R.; Jokela, N.; Vuorinen, A. Holographic quark matter and neutron stars. *Phys. Rev. Lett.* **2016**, *117*, 032501. [[CrossRef](#)] [[PubMed](#)]
- [12] Hoyos, C.; Jokela, N.; Rodríguez Fernández, D.; Vuorinen, A. Breaking the sound barrier in AdS/CFT. *Phys. Rev. D* **2016**, *94*, 106008. [[CrossRef](#)]
- [13] Annala, E.; Ecker, C.; Hoyos, C.; Jokela, N.; Rodríguez Fernández, D.; Vuorinen, A. Holographic compact stars meet gravitational wave constraints. *J. High Energy Phys.* **2018**, *12*, 078. [[CrossRef](#)]
- [14] Fadafan, K.B.; Rojas, J.C.; Evans, N. Deconfined, Massive Quark Phase at High Density and Compact Stars: A Holographic Study. *Phys. Rev. D* **2020**, *101*, 126005. [[CrossRef](#)]
- [15] Zhang, L.; Huang, M. Holographic cold dense matter constrained by neutron stars. *Phys. Rev. D* **2022**, *106*, 096028. [[CrossRef](#)]
- [16] Bitaghsir Fadafan, K.; Cruz Rojas, J.; Evans, N. Holographic quark matter with colour superconductivity and a stiff equation of state for compact stars. *Phys. Rev. D* **2021**, *103*, 026012. [[CrossRef](#)]
- [17] Annala, E.; Gorda, T.; Kurkela, A.; Nättilä, J.; Vuorinen, A. Evidence for quark-matter cores in massive neutron stars. *Nat. Phys.* **2020**, *16*, 907–910. [[CrossRef](#)]
- [18] Han, M.-Z.; Huang, Y.-J.; Tang, S.-P.; Fan, Y.-Z. Plausible presence of new state in neutron stars with masses above 0.98MTOV. *Sci. Bull.* **2023**, *68*, 913–919. [[CrossRef](#)]
- [19] Fan, Y.-Z.; Han, M.-Z.; Jiang, J.-L.; Shao, D.-S.; Tang, S.-P. Maximum gravitational mass  $M_{\text{TOV}} = 2.25 - 0.07 + 0.08 M_{\odot}$  inferred at about 3% precision with multimessenger data of neutron stars. *Phys. Rev. D* **2024**, *109*, 043052. [[CrossRef](#)]
- [20] Kurkela, A.; Romatschke, P.; Vuorinen, A. Cold Quark Matter. *Phys. Rev. D* **2010**, *81*, 105021. [[CrossRef](#)]
- [21] Chen, L.-F.; Yuan, H.-Y.; Zhou, M.-H.; Lu, K.; Wu, J.-Y.; Zhang, K. Observing Hot Holographic Quark Star with Gravitational Waves. *arXiv* **2025**, arXiv:2501.17121 .
- [22] Rougemont, R.; Grefa, J.; Hippert, M.; Noronha, J.; Noronha-Hostler, J.; Portillo, I.; Ratti, C. Hot QCD phase diagram from holographic Einstein–Maxwell–Dilaton models. *Prog. Part. Nucl. Phys.* **2024**, *135*, 104093. [[CrossRef](#)]
- [23] Cai, R.-G.; He, S.; Li, L.; Wang, Y.-X. Probing QCD critical point and induced gravitational wave by black hole physics. *Phys. Rev. D* **2022**, *106*, L121902. [[CrossRef](#)]
- [24] DeWolfe, O.; Gubser, S.S.; Rosen, C. A holographic critical point. *Phys. Rev. D* **2011**, *83*, 086005. [[CrossRef](#)]
- [25] Bazavov, A. et al. [HotQCD Collaboration]. Equation of state in (2+1)-flavor QCD. *Phys. Rev. D* **2014**, *90*, 094503. [[CrossRef](#)]
- [26] Borsányi, S.; Fodor, Z.; Guenther, J.N.; Kara, R.; Katz, S.D.; Parotto, P.; Pásztor, A.; Ratti, C.; Szabó, K.K. Lattice QCD equation of state at finite chemical potential from an alternative expansion scheme. *Phys. Rev. Lett.* **2021**, *126*, 232001. [[CrossRef](#)]
- [27] Zhao, Y.-Q.; He, S.; Hou, D.; Li, L.; Li, Z. Phase structure and critical phenomena in two-flavor QCD by holography. *Phys. Rev. D* **2024**, *109*, 086015. [[CrossRef](#)]
- [28] Burger, F.; Ilgenfritz, E.M.; Lombardo, M.P.; Müller-Preussker, M.; [tmfT Collaboration]. Equation of state of quark-gluon matter from lattice QCD with two flavors of twisted mass Wilson fermions. *Phys. Rev. D* **2015**, *91*, 074504. [[CrossRef](#)]

- [29] Datta, S.; Gavai, R.V.; Gupta, S. Quark number susceptibilities and equation of state at finite chemical potential in staggered QCD with  $N_t = 8$ . *Phys. Rev. D* **2017**, *95*, 054512. [[CrossRef](#)]
- [30] Witten, E. Cosmic Separation of Phases. *Phys. Rev. D* **1984**, *30*, 272–285. [[CrossRef](#)]
- [31] Holdom, B.; Ren, J.; Zhang, C. Quark matter may not be strange. *Phys. Rev. Lett.* **2018**, *120*, 222001. [[CrossRef](#)] [[PubMed](#)]
- [32] Blaschke, D.; Grigorian, H.; Poghosyan, G.S.; Roberts, C.D.; Schmidt, S.M. A Dynamical, confining model and hot quark stars. *Phys. Lett. B* **1999**, *450*, 207–214. [[CrossRef](#)]
- [33] Maiti, R.; Chatterjee, D. Investigating the role of nuclear parameters in Neutron Star oscillations: A model comparison. *Phys. Rev. D* **2025**, *111*, 023017. [[CrossRef](#)]
- [34] Kettner, C.; Weber, F.; Weigel, M.K.; Glendenning, N.K. Structure and stability of strange and charm stars at finite temperatures. *Phys. Rev. D* **1995**, *51*, 1440. [[CrossRef](#)]
- [35] Sekiguchi, Y.; Kiuchi, K.; Kyutoku, K.; Shibata, M. Effects of hyperons in binary neutron star mergers. *Phys. Rev. Lett.* **2011**, *107*, 211101. [[CrossRef](#)]
- [36] Drago, A.; Pagliara, G. The scenario of two families of compact stars: 2. Transition from hadronic to quark matter and explosive phenomena. *Eur. Phys. J. A* **2016**, *52*, 41. [[CrossRef](#)]
- [37] Yagi, K.; Yunes, N. I-Love-Q. *Science* **2013**, *341*, 365–368. [[CrossRef](#)]
- [38] Yagi, K.; Yunes, N. I-love-q relations in neutron stars and their applications to astrophysics, gravitational waves, and fundamental physics. *Phys. Rev. D* **2013**, *88*, 023009. [[CrossRef](#)]
- [39] Silva, H.O.; Yunes, N. I-love-q to the extreme. *Class. Quantum Gravity* **2017**, *35*, 015005. [[CrossRef](#)]
- [40] Adam, C.; Martín-Caro, A.G.; Huidobro, M.; Vázquez, R.; Wereszczynski, A. Quasiuniversal relations for generalized skyrme stars. *Phys. Rev. D* **2021**, *103*, 023022. [[CrossRef](#)]
- [41] Li, J.J.; Sedrakian, A.; Weber, F. Universal relations for compact stars with heavy baryons. *Phys. Rev. C* **2023**, *108*, 025810. [[CrossRef](#)]
- [42] Atta, D.; Singh, V.; Basu, D.N. Universal relationships for neutron stars from perturbative approach. *arXiv* **2024**, arXiv:2408.00646. [[CrossRef](#)]
- [43] Kumar, A.; Ghosh, M.K.; Thakur, P.; Thapa, V.B.; Nath, K.K.; Sinha, M. Universal relations for compact stars with exotic degrees of freedom. *Eur. Phys. J. C* **2024**, *84*, 692. [[CrossRef](#)]
- [44] Pani, P. I-Love-Q relations for gravastars and the approach to the black-hole limit. *Phys. Rev. D* **2015**, *92*, 124030. [[CrossRef](#)]
- [45] Martinon, G.; Maselli, A.; Gualtieri, L.; Ferrari, V. Rotating protoneutron stars: Spin evolution, maximum mass, and i-love-q relations, *Phys. Rev. D* **2014**, *90*, 064026. [[CrossRef](#)]
- [46] Lau, S.; Leung, P.; Lin, L.-M. Two-layer compact stars with crystalline quark matter: Screening effect on the tidal deformability. *Phys. Rev. D* **2019**, *99*, 023018. [[CrossRef](#)]
- [47] Raduta, A.R.; Oertel, M.; Sedrakian, A. Proto-neutron stars with heavy baryons and universal relations. *Mon. Not. R. Astron. Soc.* **2020**, *499*, 914–931. [[CrossRef](#)]

- [48] Burikham, P.; Pinkanjanarod, S.; Ponglertsakul, S. Slowly rotating neutron star with holographic multi-quark core: I-love-q relations. *Phys. Rev. D* **2022**, *105*, 104018. [[CrossRef](#)]
- [49] Roy, S.K.; Chaudhuri, G. I-c-q relations for rapidly rotating stable hybrid stars. *Astropart. Phys.* **2025**, *170*, 103108. [[CrossRef](#)]
- [50] Wu, J.-Y.; Li, W.; Huang, X.-H.; Zhang, K. Dark I-Love-Q. *arXiv* **2025**, arXiv:2309.07971. [[CrossRef](#)]
- [51] Zhang, K.; Huang, G.-Z.; Tsao, J.-S.; Lin, F.-L. GW170817 and GW190425 as hybrid stars of dark and nuclear matter. *Eur. Phys. J. C* **2022**, *82*, 366. [[CrossRef](#)]
- [52] Meltzer, D.W.; Thorne, K.S. Normal Modes of Radial Pulsation of Stars at the End Point of Thermonuclear Evolution. *Astrophys. J.* **1966**, *145*, 514. [[CrossRef](#)]
- [53] Borsanyi, S.; Fodor, Z.; Guenther, J.N.; Kara, R.; Katz, S.D.; Parotto, P.; Pasztor, A.; Ratti, C.; Szabo, K.K. QCD Crossover at Finite Chemical Potential from Lattice Simulations. *Phys. Rev. Lett.* **2020**, *125*, 052001. [[CrossRef](#)] [[PubMed](#)]